

SEA ICE INDENTATION IN THE CREEPING MODE

by Fadi S. Chehayeb, Seng-Kiong Ting, S. Shyam Sunder
and Jerome J. Connor,

Massachusetts Institute of Technology



Copyright 1985 Offshore Technology Conference

This paper was presented at the 17th Annual OTC in Houston, Texas, May 6-9, 1985. The material is subject to correction by the author. Permission to copy is restricted to an abstract of not more than 300 words.

ABSTRACT

A finite element method of analysis is developed and applied to the study of global and local pressures generated on a cylindrical indenter during sea ice deformations in the creeping mode. Numerical simulations are performed under plane stress conditions to assess the influence of interface adfreeze and friction, material constants for a multi-axial power-law creep model, indenter diameter, and ice sheet velocity on predicted pressures. The results are compared with those based on approximate methods of analysis. Stress, strainrate and strain contours are obtained in addition to the distribution of interface pressures.

INTRODUCTION

Extraction of hydrocarbons from the Arctic offshore requires the design of drilling and production platforms to withstand loading generated by perennial ice features. Two levels of loading are typically considered; Global ice forces govern the overall structural geometry and dimensions as well as the foundation design while local pressures are likely to dictate wall thicknesses and local framing, and may well govern structural cost.

The interaction of an ice sheet with a vertically faced (and usually rigid) indenter is an important loading condition for cylindrical structures and for conical structures with grounded rubble pile or accreted ice foot. In general, this indentation phenomenon is characterized by the simultaneous occurrence of viscous (rate-dependent) and fracture behavior.

Several theoretical models based on approximate methods of analysis that idealize the ice sheet as a continuum have been proposed for predicting global ice forces. These include: (1) the upper and lower bound, plasticity type solutions of Michel and Toussaint¹, Croasdale et al.², and Ralston³, (2) the reference stress, power law creep solution of Ponter et al.⁴, and (3) the upper bound, power law creep solutions of Bruen, Vivatrat and Chen^{5,6}, and Ting and Shyam Sunder⁷. The plasticity type models require empirical definition of an average strain rate measure

to account for the viscous behavior of ice, the reference stress approach accounts for the effect of variability in material constants in an approximate sense, and the upper bound, power law creep solutions require accurate specification of ice sheet kinematics. No equivalent theoretical models exist for the case where either pure (linear elastic) fracture or combined viscous and fracture effects dominate.

Theoretical predictions of interface pressures are not generally available. However, Ting and Shyam Sunder⁷ have applied the (approximate) strain path method of analysis, originally developed for deep penetration problems in soil mechanics by Baligh⁸, to study interface pressures during plane strain indentation. Their results for a power law creep model of ice showed that normal interface pressures may be 0.5-1 times the global pressure. They also found that interface adfreeze and friction stresses can significantly influence ice pressures.

The "continuum" predictions of ice pressures may in many cases be too high by a factor of 2-10. Four major factors can explain this uncertainty: (i) incomplete modeling of the mechanical behavior of ice, including temperature and fracture effects, (ii) empiricism in the theoretical models resulting from the use of approximate analysis methods, (iii) inadequate modeling of contact forces at the ice-structure interface, and (iv) ignoring the effects of size on material strength.

A study of ice indentation in the creeping mode is important for two reasons: (a) creep is the pre-dominant mode of deformation for artificial islands in the Arctic nearshore region during "breakout" and/or steady indentation conditions occurring in the winter, and (b) stresses, strains, and strainrates within the continuum resulting from creep are necessary to predict the initiation and possibly even the propagation of cracks when viscous effects influence fracture behavior. In a recent paper, Shyam Sunder and Ting⁹ have shown that a limiting tensile strain criterion dependent on the instantaneous strainrate can explain crack initiation in ice. Furthermore, for load transmitting systems such as ice features (as opposed to load bearing structural systems) the use of this criterion for fracture propagation is likely to be

conservative when compared to a classical fracture mechanics approach. This is because the latter considers only the propagation of pre-existing cracks with a given distribution of sizes, while the former may be used to predict both the initiation and propagation of cracks in a material originally in virgin (flawless) form.

This paper is concerned with the development and application of a finite element method of analysis for studying global and local pressures generated on a rigid, cylindrical indenter during sea ice deformations in the creeping mode. Numerical simulations are performed under plane stress conditions to assess the influence of interface adfreeze and friction, material constants for a multi-axial power law creep model, indenter diameter, and ice sheet velocity on predicted pressures. The results are compared with those based on approximate methods of analysis. Stress, strain-rate, and strain contours are obtained in addition to the distribution of interface pressures.

FINITE ELEMENT FORMULATION

Governing Equations.-- For general viscoplastic behavior, which includes creep, it is convenient to work with time derivatives of the governing equations for a solid. The weighted equilibrium-rate equation which forms the basis for the finite element displacement method is then given by:

$$\int \underline{B}^T \underline{\dot{\sigma}} dV = \dot{\underline{P}} \quad (1)$$

where \underline{B} is the strainrate - nodal velocity transformation matrix derived from the chosen displacement expansion for the finite element, i.e.,

$$\underline{\dot{\epsilon}} = \underline{B} \underline{\dot{U}} \quad (2)$$

The strainrate vector consists of two components, one due to elastic strains, characterized by the compliance matrix \underline{C} and its inverse the rigidity matrix \underline{D} , and the other due to inelastic (irrecoverable) strains.

$$\underline{\dot{\epsilon}} = \underline{C} \underline{\dot{\sigma}} + \underline{\dot{\epsilon}}_I \quad (3)$$

where I refers to the inelastic strains. For linearly elastic behavior, the compliance and rigidity matrices do not vary in time. The inelastic component may consist of rate-independent plastic strains, permanent creep (nonlinear viscoelastic) strains, and/or viscoplastic strains. In general, this may be expressed as:

$$\underline{\dot{\epsilon}}_I = f(\underline{\sigma}, \underline{\dot{\sigma}}, \underline{\epsilon}_I, T) \quad (4)$$

where T allows for temperature dependence.

Combining Eqs. (1)-(3) and defining \underline{K} as the elastic stiffness matrix of the element leads to the element equilibrium equation:

$$\underline{K} \underline{\dot{U}} = \dot{\underline{P}} + \int \underline{B}^T \underline{D} \underline{\dot{\epsilon}}_I dV \quad (5)$$

and the element stressrate - nodal velocity relations:

$$\underline{\dot{\sigma}} = \underline{D} \underline{B} \underline{\dot{U}} - \underline{D} \underline{\dot{\epsilon}}_I \quad (6)$$

The global stiffness matrix, \underline{K}_G , is obtained from Eq. (5) using conventional procedures.

Material Modeling.-- In this paper, sea ice is treated as a linearly elastic plus creeping material. Thus, \underline{K} is the element stiffness matrix usually employed in linear elastic analyses. Under uniaxial (compressive) loading conditions, creep in ice is generally expressed in terms of a power law¹⁰, i.e.,

$$\dot{\epsilon}_c = a \sigma^N \quad (7)$$

where a and N are constants with the temperature dependence being included in the parameter a following an Arrhenius activation energy law.

The multi-axial generalization of the creep law as proposed by Palmer¹¹ is based on assuming incompressibility, which is valid for ice as long as the hydrostatic stress is not too high such as under plane stress conditions. It suffices then to relate the creep strainrate tensor to the deviatoric stress tensor. This is accomplished by assuming that the two tensors are directly proportional to one another as given by the associative flow rule:

$$\underline{\dot{\epsilon}}_c = \lambda \underline{S} \quad (8)$$

where λ is a scalar parameter and \underline{S} is a vector containing the deviatoric stresses. For a von Mises (isotropic) yielding surface, λ is the ratio of the octahedral shear strainrate to the octahedral shear stress. For the uniaxial power law given in Eq. (7), it follows that:

$$\lambda = 3/2 a \sigma_e^{N-1} \quad (9)$$

with the effective stress measure σ_e defined as:

$$\sigma_e = (3/2 S_{ij} S_{ij})^{1/2} \quad (10)$$

* Given the stress vector, the deviatoric stresses may be obtained by subtracting the hydrostatic stress, i.e., $\underline{S} = \underline{G} \underline{\sigma}$ in matrix form. Then applying Eqs. (10), (9), and (8) in succession leads to the creep strainrate vector.

Solution Algorithm.-- An iterative solution algorithm is developed to solve a pseudo-force form of the nonlinear governing equations given in Eqs. (5) and (6). Although the algorithm has been applied to the specific material model presented above, it can be easily generalized to account for material anisotropy and for cracking based on the limiting tensile strain criterion. For purposes of discussion, attention is focussed at the element rather than the global level. At first the governing equations are integrated in time between t_i and t_{i+1} to yield:

$$\underline{K}(\underline{U}_{i+1} - \underline{U}_i) = \underline{P}_{i+1} - \underline{P}_i + \int \underline{B}^T \underline{D} (\underline{\epsilon}_{c,i+1} - \underline{\epsilon}_{c,i}) dV \quad (11)$$

$$\underline{\sigma}_{i+1} - \underline{\sigma}_i = \underline{D} \underline{B} (\underline{U}_{i+1} - \underline{U}_i) - \underline{D} (\underline{\epsilon}_{c,i+1} - \underline{\epsilon}_{c,i}) \quad (12)$$

Creep strains which appear in both the equations are nonlinear functions of stress since λ in Eq. (8) is not a constant. A two-level iterative algorithm is used to solve these equations for each new time step t_{i+1} . The key steps in the solution algorithm are as follows:

1. Compute the displacement increments from (the global form of) Eq. (11) for the given loading vector. In the first iteration on the equation, the incremental creep strains are assumed to be zero.

2. Compute the incremental stresses and incremental creep strains from Eq. (12) for the displacement increments obtained in step 1 using the iterative algorithm (lower-level iteration in k) discussed below. In the first iteration on this equation assume the incremental creep strains to be zero.
3. Return to step 1 and iterate on Eq. (11) (higher-level iteration in j) using the incremental creep strains obtained in step 2 until convergence is achieved. Two convergence criteria are used: (a) ratio of norm of displacement increment vector to norm of displacement vector at given time step is less-than-or-equal-to 0.001; and (b) absolute value of energy norm is less-than-or-equal-to 0.001, i.e.,

$$\left| \frac{\Delta \underline{p}^j \cdot \Delta \underline{u}^j}{\Delta \underline{p}^0 \cdot \Delta \underline{u}^0} \right| < 0.001 \quad (13)$$

where $\Delta \underline{p}$ refers to the entire right hand side of Eq. (11). The evaluation of the integral defining the inelastic load vector is based on a Gaussian quadrature formula (for a four-noded quadrilateral element, four integration points are used). Typically, 4-6 iterations are required for convergence at the higher-level.

The evaluation of the incremental stresses and incremental creep strains in step 2 requires the simultaneous consideration of Eqs. (12) and (8). In addition to a nonlinear equation solver, a numerical time integrator is needed to obtain results. Previous investigators^{12,13,14} have used a simple successive substitution type algorithm to decouple the two equations. This involves the use of incremental creep strains from iteration k to evaluate the incremental stresses for iteration k+1 using Eq. (12). The incremental creep strains for iteration k+1 are then evaluated with the α -method of numerical time integration which expresses Eq. (8) as:

$$(\underline{\epsilon}_{c,i+1} - \underline{\epsilon}_{c,i}) = \lambda \alpha \underline{S}_\alpha (t_{i+1} - t_i) \quad (14)$$

where \underline{S}_α is a weighted average of the deviatoric stress vector in the time interval $(t_{i+1} - t_i)$ and $\lambda \alpha$ is derived from a similar weighting on the effective stress, i.e.,

$$\underline{S}_\alpha = (1-\alpha) \underline{S}_i + \alpha \underline{S}_{i+1} \quad (15)$$

Typical values of α lie in the range 0-1. A value of α equal to zero yields the forward (explicit) Euler method, while α equal to one yields the backward (implicit) Euler method. Both these formulas are first-order accurate (for linear problems in which λ is a constant, and not dependent on the effective stress), although the actual error of the backward formula is considerably less than that of the forward formula assuming that the former is iterated up to convergence. A value of α equal to 0.5 yields the well-known trapezoidal rule, also called the improved Euler's method since it is second-order accurate. A linear stability analysis of the α -method shows that it is unconditionally stable only for $\alpha > 0.5$.

For quasi-elastic problems in which creep defor-

mations are not dominant, experience has shown that for small time increments $\alpha=0.5$ is more accurate, and that for large time increments $\alpha=1$ is to be preferred. However for creep dominant problems of concern here, the convergence rate slows down considerably for highly stressed elements when $\alpha=1$ is used, and more than 10-12 iterations may be needed for convergence at the lower-level. This is computationally unattractive since iteration is necessary at each integration point within an element (four in the case of a quadrilateral element) and highly stressed elements may occur often in a large finite element grid, e.g., consisting 250 elements.

Convergence is accelerated here by developing a lower-level algorithm that combines a Newton-Raphson or tangent type iteration with the α -method. The resulting equations are listed below:

$$\left[\underline{I} + \underline{D} \frac{\partial \Delta \underline{\epsilon}}{\partial \underline{\sigma}} \right]_{-i+1}^k \underline{\sigma}_{-i+1}^{k+1} = \underline{\sigma}_{-i+1}^k + \underline{D} [\underline{B} \Delta \underline{u} - \Delta \underline{\epsilon}_{-i+1}^k] + \underline{D} \left[\frac{\partial \Delta \underline{\epsilon}}{\partial \underline{\sigma}} \right]_{-i+1}^k \underline{\sigma}_{-i+1}^k \quad (16)$$

where $\Delta \underline{\epsilon}_{-i+1}^k$ is obtained by applying Eq. (14) after obtaining the stress quantities at iteration k, and similarly:

$$\left[\frac{\partial \Delta \underline{\epsilon}}{\partial \underline{\sigma}} \right]_{-i+1}^k = \Delta t \alpha \left[\lambda \underline{I} + \frac{3}{2} \sigma_e^{-1} \frac{\partial \lambda}{\partial \sigma_e} \underline{S} \underline{S}^T \right]_{-i+1}^k \underline{G} \quad (17)$$

For the given material model, $\partial \lambda / \partial \sigma_e$ can be obtained from Eq. (9). Notice that the algorithm becomes explicit for $\alpha=0$ as it should and no iteration is required. Convergence is defined to occur when the maximum absolute value of the relative change in point stresses between iteration k and k+1 is less-than-or-equal-to 0.001. Iteration is also stopped if the actual point stresses are zero at k and their maximum absolute value is less-than-or-equal-to 0.001 at k+1. Application of this iterative scheme with $\alpha=1$ shows that convergence is typically obtained in 4 iterations instead of more than 10-12, thereby cutting down the computational effort by approximately 50% if the increased computational effort per iteration is accounted for.

Computer Implementation.-- The finite element analysis algorithm has been implemented in a computer code called DECNEC (Discrete Element Computational NEtwork Controller). Data input is simplified by the use of a pre-processor specially written for the program. A post-processor called ORION, originally developed at the Lawrence Livermore Laboratory, can produce graphical display of stress, strain, and strainrate contours as well as interface pressure distributions.

The current implementation is a two-dimensional version for plane stress problems, while the development of a plane strain version is underway. A four-noded quadrilateral element is currently available. Although an eight-noded quadratic element is often preferred (and will be included in the future), accurate results can and have been obtained with the four-noded element using a finer finite element mesh. The program has the ability to simulate a free or frictional contact between two deformable bodies, i.e., no contact stresses due to adfreeze bond, by defining the interface as a "slideline".

Code Verification.-- The accuracy of the computer code has been verified in two ways; through the solution of simple test problems, and by comparing (see subsequent section) the variability in predicted global pressures due to indenter diameter, material model parameters, and ice sheet velocity with that predicted by approximate methods of analysis. In both cases, the numerical solutions are accurate to within specified tolerances typically achievable in finite element analyses.

One of the test problems, for example, considers a two-dimensional rectangular element subjected to a uniform compressive stress ($\sigma_z = -\sigma$) normal to one of its sides and with normal movement constrained on the other three sides (Fig. 1). A simple analysis shows that for the given material model, the lateral stress (σ_y) is given by:

$$\sigma_y = -\sigma_z/2 [(1-2\nu)e^{-2/3E\lambda t} - 1] \quad (18)$$

where ν is the Poisson's ratio and E is the Young's modulus. This solution is valid for a constant value of λ , which in an average sense may be defined as its value at steady state. Under steady state conditions, i.e., large t , Eq. (18) shows that the lateral stress is compressive and equal to half the z -stress. Furthermore, the z -strainrate is the creep strainrate and equals $-1/2 \lambda \sigma$ while the lateral strainrate is zero as it should be for the given boundary conditions. Application of DECNEC using two finite elements verified this analysis.

NUMERICAL SIMULATIONS

Description of Case Studies.-- Numerical simulations are performed for the seven cases identified in Table 1. The objectives of the first three simulations are to quantify the effect of interface adfreeze and friction on predicted indentation pressures. The fixed condition provides an upper bound solution since the ice-structure interface is considered to be infinitely strong. The free condition corresponds to no adfreeze bond and interface friction, while the roller condition provides an intermediate solution. The next two simulations study the influence of ice sheet velocity on pressures. The chosen base velocity of 0.195 m/hr corresponds to the recorded maximum average velocity over a twelve-hour period just prior to "breakout" (macrocracking) for an artificial island in the Beaufort Sea. The sixth simulation attempts to quantify the effect of a grounded rubble pile or an accreted ice foot on ice pressures by defining a larger effective indenter diameter (2.85 times the structural diameter). The final simulation studies the effect of variability in constants defining the material model on ice pressures. Two sets of parameters for sea ice based on the work of Sanderson¹⁵ and Wang¹⁶, respectively, are considered: $N=3$, $a=2.125 \times 10^{-6}$ (MPa)⁻³s⁻¹; and $N=4$, $a=1.848 \times 10^{-6}$ (MPa)⁻⁴s⁻¹. The elastic constants, which have negligible influence on the steady state solutions, are taken to be $E=9.5$ GPa and $\nu=0.3$.

Numerical Implementation.-- Prior to carrying out the above studies, it is necessary to set up the finite element mesh, specify a time increment for the analysis, and define the excitation.

The finite element mesh is defined such that (i) the aspect ratio of each element is as close to one as possible, (ii) the scatter in stresses predicted by adjacent elements at their common boundary is less

than 10%, and (iii) the boundary of the ice sheet is a circle whose extent is sufficient to simulate the infinite medium. The first criterion is maintained by the pre-processor which makes the radial length of each element equal to its arc length nearer the indenter. The second criterion is controlled by specifying the number of radial segments into which a quarter-plane may be divided. A value of nine is considered here (for an eight-noded element five or six may suffice). The last criterion is also implemented by the pre-processor which makes the radius of the circular boundary equal to 9.5 times the indenter radius. Accounting for symmetry about the z -axis, the above discretization leads to a finite element mesh with 252 elements and 285 nodal points (Fig. 2). The number of degrees-of-freedom is 476 for the fixed condition, 538 for the roller condition, and 540 for the free condition.

The choice of time increment is made to satisfy the conflicting requirements of accuracy and computational effort. Accuracy, in turn, is achieved by allowing sufficient time for the solution to reach steady state and by specifying a time increment that captures the variability in response prior to reaching steady state. Experience with the simulations has shown that it is appropriate to consider a time increment which makes the exponent in Eq. (18) equal to 40 in 20 time steps. For typical values of λ and E , the time increment is approximately 100 s.

The chosen uniform far-field velocity listed in Table 1 defines the excitation here, although other types of excitation such as environmental traction on the ice sheet can be handled equally well. For a given time step, the excitation is defined in terms of an imposed displacement in the z -direction at the far-field boundary nodes. This displacement value is made to increase linearly in time, consistent with the chosen uniform velocity.

DISCUSSION OF RESULTS

Global Forces.-- Table 2 lists the global pressures predicted by the finite element analysis for the seven cases of interest. Pressure values are the global forces divided by the indenter diameter D , and ice sheet thickness t .

Comparing the first three values of global pressure it is seen that the fixed condition does provide an upper bound solution. The global pressure for the fixed case is about 28% higher than that for the roller case. In turn, the global pressure for the roller case is 1.93 or almost twice that for the free case. This spread in global pressures is indicative of the influence of interface friction and adfreeze bond. The hundred percent reduction in pressure between the roller and free case can be explained by examining the stresses within the ice sheet. For the roller case, the upstream and downstream stresses are equal in magnitude and their resultants act together in the z -direction. In the free case, the downstream stresses are almost zero since the lack of contact at the interface on this side tends to eliminate any influence of the indenter on the ice sheet. As a result, the downstream part of the ice sheet acts predominantly like a rigid body. This tends to reduce global pressures by almost a half.

The fourth and fifth values of global pressure indicate that reducing the ice sheet velocity by a factor of 6.4 leads to a 46% reduction in pressures

while increasing the velocity by a factor of 1.6 leads to a 17% increase in pressures. Thus even a factor of two uncertainty in velocity will affect the pressures only by about 20-30%.

Cases 2 and 6 provide some idea of the effect of a grounded rubble pile or an accreted ice foot. By defining an effective indenter diameter equal to 2.85 times the structural diameter, the global pressure has reduced by 31%. However, the global force has actually increased by 97% from 211 MN/(unit ice thickness) for case 2. Two extreme scenarios can be considered to estimate the global force felt by the structure when there is a grounded rubble pile: (i) the entire global force is transmitted to the structure which in turn transmits it to the foundation, and (ii) both the structure and the grounded rubble pile resist the global force, each transmitting to the foundation a force proportional to its contact area with the foundation. Under the first scenario, which is probably overconservative, the global force on the structure is 414 MN/(unit ice thickness) an increase of 97% from case 2. Under the second scenario, which may be reasonable only if the rubble pile is consolidated and grounded firmly in the foundation soil such as in the case of constructed ice packs, the global force on the structure is 51 MN/(unit ice thickness) a reduction of 76% from case 2. Further research is necessary to quantify the level of force that can be directly transmitted to the foundation by a grounded rubble pile.

The last case shows that the two sets of material constants considered in this paper lead to ice pressures which differ by about 19%. Combining this information with earlier experience indicates that uncertainties in material constants for an isotropic power law creep model may yield ice pressures that vary by about 15-30%. However, improved material models that include fracture and temperature effects in addition to the transversely isotropic behavior of sheet ice can have a major influence on ice pressure predictions.

Calibration with Approximate Solutions.-- The global pressures for cases 4 through 7 indicate the influence of ice sheet velocity V , indenter diameter D , and material constants a and N on the results. In order to provide perspective and calibration with solutions based on approximate methods of analysis, the upper bound solution of Ting and Shyam Sunder⁷ corresponding to a two-dimensional velocity field obtained by superposing a uniform flow and a doublet, is considered. The resulting kinematic model resembles the flow of an infinite ice sheet past a circular indenter with the interface matching most the roller condition. According to the solution, the global pressure is proportional to $(V/D)^{1/N}$. If this variation is valid, the ratio of global pressures in cases 4 through 6 to case 2 should be 0.54, 1.16 and 0.70, respectively. The finite element analysis predicts the ratios to be 0.54, 1.17 and 0.69. For the two sets of material constants in cases 7 and 2, the approximate solution predicts a ratio of 1.17 while the finite element analysis predicts a ratio of 1.19. In all cases, the effect of changes in V , D , a and N on the finite element solutions is almost identical to that predicted by the upper bound, creep law solution.

In order to compare the actual (as opposed to ratios of) global pressures, it is necessary to recognize that the two-dimensional nature of the chosen kinematic field makes the approximate analysis

strictly correspond to a plane strain condition and not a plane stress condition. Ponter et al.'s⁴ analysis for both plane strain and plane stress based on the reference stress method can be used to derive a correction factor by which to divide the approximate solution for applying it under plane stress conditions. For the material model with $N=3$ the correction factor is 1.8 and for the $N=4$ model it is 1.96. The approximate formula corrected by a rounded factor of 2 is given below:

$$\frac{P}{Dt} = \frac{2\pi}{\sqrt{3}} \frac{N}{N+3} \left[\frac{4}{\sqrt{3}} \frac{1}{a} \frac{2V}{D} \right]^{1/N} \quad (19)$$

where the quantity in brackets raised to the power of $1/N$ may be interpreted as the uniaxial strength of ice evaluated at an average effective strainrate of $8/\sqrt{3}$ V/D using Eq. (7). Table 2 shows that the predictions based on Eq. (19) differ from the finite element solutions by less than 10%. The fixed condition is obtained by multiplying the above equation by 1.3, while the free condition uses a multiplying factor of 0.5 (Table 3). Note that (i) the uncorrected upper bound solutions are overconservative by almost hundred percent or more, and (ii) the approximate solutions need no longer be upper bounds once the correction factor is applied.

Local Pressures.-- The maximum (peak) interface normal stress for each of the seven simulations is listed in Table 2. The table also lists a maximum interface shear stress of 0.73 MPa for the fixed condition. There are no interface shear stresses for the roller and free conditions. Notice that in all cases the maximum normal pressure is approximately 0.35-1.10 times the global pressure, and not several (e.g., three) times the global pressure.

The maximum normal stress for the fixed condition is lower than that for the roller condition by 17%, although a reverse trend is observed for global pressures. This occurs because part of the force in the fixed condition is carried by interface shear stress. On the other hand, the maximum normal stress for the free condition is about 4% higher than that for the roller condition. There are no interface stresses on the downstream side for the free condition due to lack of contact between the ice sheet and the indenter. The small level of stresses that exist in the predominantly rigid continuum on the downstream side are transmitted to the structure from the upstream side, thereby increasing the normal stresses on that side by the 4% mentioned above.

Comparison of the local and global pressures shows that the ratio of the maximum normal interface stress to the global pressure is approximately 0.35 for the fixed condition, 0.55 for the roller condition, and 1.10 for the free condition. Furthermore, the variation of local pressures with V , D , a and N is similar to that for global pressures. Thus multiplication of Eq. (19) by 0.46, 0.55, and 0.55 can be used to estimate the respective maximum normal pressures (Table 3). In a similar fashion, the maximum interface shear stress for the fixed condition may be estimated from the equation with a multiplication factor of 0.37.

For purposes of design it is necessary to consider not only the maximum values of normal stress but also its distribution on the structure. The design of

individual structural components is typically based on a tributary loaded area. It is possible that the average integrated stress on this area due to contact with the ice sheet is significantly less than the point maxima of stress. Further, the average stress may reduce for structural components which have larger tributary areas. Figures 3 and 4 present the normal stress distributions on the interface. Note that the normal stresses are always zero where the indenter is tangential to the direction of ice sheet movement (i.e., angle equal to zero degrees). At the end of the first time step where the solution is predominantly elastic, the distributions are cosinusoidal as one may expect. However as steady state is reached, there is a tendency for the distributions to become rectangular or uniform. The distribution is more rectangular for the free and roller conditions than for the fixed condition which appears to be predominantly cosinusoidal due to lower stress levels, as well as for the $N=4$ case than for the $N=3$ case since an increasing value of N makes the ice behave more like a rigid-plastic material. The figures also show that downstream interface stresses are zero for the free condition. The distributions are not affected, at least visually, as V and D are varied, although they have to be scaled according to the maximum normal stresses in Table 2. A conservative design approach may be to assume a uniform distribution of stresses based on the maximum normal interface stress.

A careful consideration of the interface stress levels sheds some light on which of the three conditions, fixed, roller or free, is realistic. Figure 5 shows the distribution of interface shear stresses for the fixed condition. At steady state, the distribution is predominantly sinusoidal with the maximum value of 0.73 MPa occurring at the tangent point. The shear strength of adfreeze bond and sea ice as reported in the literature^{17,18} varies over a wide range 0.02-1.38 MPa. It is very likely that either the adfreeze bond will give way or the ice will fracture in shear over a significant fraction of the indenter perimeter. In addition, for the typical range of effective strainrates close to the downstream tip of the indenter, the tensile strength of ice is less than the downstream normal interface stresses for the fixed and roller conditions, both of which are tensile. Once again, if the adfreeze bond does not give way, a tensile fracture may occur in the ice over the perimeter close to the interface on the downstream side. Thus, for local pressures the use of the free condition should be preferred. The choice will be conservative over the fixed condition and, marginally so, over the roller condition. However, the free condition may be unconservative for global pressures if the indentation problem is one in which the structure is surrounded by an infinite ice sheet and it is possible for frictional stresses or adfreeze bond to develop at the interface.

Comparison with Pressure-Area Curves.-- Pressure-area curves are often constructed to help designers obtain the average pressures over tributary loaded areas for structural components¹⁹. A typical curve developed by Sanderson²⁰ is shown in Fig. 6. The darkly shaded areas on the figure correspond to actual measurements of ice pressure under widely varying conditions, while the lightly shaded areas represent the author's extrapolation of the measurements. The dark regions in the extreme left are from laboratory indentation tests such as those of Frederking and Gold²¹, and Micheland Toussaint¹. The central region reflects measurements from ice breakers traveling in

the Arctic, while the two smaller regions on the right correspond to global forces on artificial islands estimated from pressure sensor measurements in the ice sheet. The contact area is defined as the indenter area of contact for the laboratory and artificial island data. For the ice breaker data, the contact area is the local area over which the pressure measurement is made and not the form area of the ice breaker. This figure shows that for an artificial island with a contact area of 200 m², the indentation pressure may be around 1 MPa. However for a local area of 10 m² on the same structure, the indentation pressure may be around 3 MPa.

The local to global pressure ratio of three obtained from the pressure-area curve seems to contradict the findings in the previous subsection. Fortunately, this is not so. If the contact area in Fig. 6 is interpreted as Dt , then a smaller contact area implies a smaller indenter diameter if the ice thickness remains unchanged. The effect of indenter diameter is well modelled by Eq. (19). A plot of the maximum normal interface pressure estimate from the equation leads to the solid line in the figure. Eq. (19) is appropriately modified to account for transition from plane stress to plane strain using Ponter et al.'s reference stress method⁴. This affects the curve, in an insignificant manner, over the region 1-10 m². When the effective strainrate, i.e., $8/\sqrt{3} V/D$, exceeds $5 \times 10^{-4} \text{ s}^{-1}$, ice is assumed to have fractured (crushed) and the uniaxial strength is capped, leading to the flat portion of the curve on the extreme left. The predicted behavior provides an excellent match to Fig. 6. Thus, a more appealing interpretation of the figure is to consider the contact area as the indenter area (Dt in our case) and not the tributary loaded area for a structural component, and the indenter pressure corresponding to a given contact area as the maximum normal interface pressure for that indenter. The distribution of the interface stresses may be assumed uniform over the indenter area of contact as concluded earlier. However, a different boundary value problem involving a smaller contact area, as opposed to contact over half the perimeter in the free condition, will lead to higher interface pressures.

The key assumption in generating the analytical curve in Fig. 6 concerns the choice of V . The value of 0.195 m/hr considered here is based on data for an artificial island just prior to "breakout" or macro-cracking, which leads to an excellent match between predicted and measured indentation pressures for the structure. However, significantly higher velocities do occur in the field for which the current predictive models based purely on an isotropic creep law will lead to increasing pressures. Fracture in ice will be the key mechanism that limits pressures generated under higher velocities.

Multiaxial Behavior of Ice Sheet.-- A study of the multiaxial behavior of an ice sheet during indentation in the creeping mode provides clues to likely failure modes, particularly fracture. All forms of fracture (crushing, spalling, splitting) initiate as a result of tensile strains perpendicular to the crack direction. Even if the applied loads at the element level are not tensile, it is possible for tensile conditions to occur in a rotated frame of reference, e.g., a 45° rotation in the case of pure shear.

Table 4 lists the principal stresses at the point of maximum interface pressure at two time instants: at the end of the first time step (around 100 s) where

the solution is predominantly elastic, and at the twentieth time step (around 2000 s or 30 minutes) where the solution has reached steady state and is predominantly creep. The biaxial stress state at the first time step is compression-tension for all the cases except for a fixed condition where it is compression-compression. As creep starts to dominate, all the cases tend to compression-compression. Figures 7 and 8 shows how this compression-compression region grows in time for the fixed and free cases. The region is much larger for the fixed condition than for the free condition. The roller condition is somewhere in between although it resembles more the free condition. The most striking observation that can be made from these figures is that tensile stresses occur almost all over the ice sheet. Biaxial tension tends to occur on the downstream side, while compression-tension states of stress are present on both sides. Experimental evidence under compression-tension states of stress²² shows that the occurrence of even small tensile stresses weakens ice considerably, leading to premature fracture when compared with uniaxial tensile loading.

Figure 9 shows the strain fields, which are more relevant to explaining fracture initiation. Since the algebraically maximum principal strains are positive (or almost so) over the entire ice sheet for the fixed and roller conditions at steady state, there is no compression-compression (and by symmetry no tension-tension) region of strain. A tension-compression state of strain dominates the ice sheet, with tensile strains exceeding 0.001 at steady state. As the tensile failure strain is about 0.001 or less for strainrates greater than 10^{-7} s^{-1} under just uniaxial loading, it seems likely that cracking will occur even before steady state creep is reached. Similar conclusions apply for the free condition, the only difference being that downstream strains are negligible.

The maximum effective strainrates for the seven simulations are listed in Table 2. For the kinematic model considered by Ting and Shyam Sunder⁷ which is closest to the roller condition, the maximum effective strainrate equals $8/\sqrt{3} \text{ V/D}$. The prediction of $2.3 \times 10^{-6} \text{ s}^{-1}$ for case 2 compares well with the finite element analysis value of $3.4 \times 10^{-6} \text{ s}^{-1}$. Further, cases 4 through 6 are consistent with the predicted proportionality to V/D . Contours of effective strainrate are plotted in Fig. 10. The strainrates tend to zero at the tangent points for the roller and free conditions as one may expect and is a maximum close to but not at the tips. On the other hand, the tangent point has the maximum value for the fixed condition. In the immediate vicinity of the indenter, these plots are different from the circular contours predicted by the kinematic model in the approximate analysis. This finding reinforces Ting and Shyam Sunder's⁷ observation that the approximate upper bound analysis is quite accurate for global pressures, although the use of the strain path method with a kinematic model that does not capture interface conditions may be inadequate for local pressure predictions.

CONCLUSIONS

This paper has presented a finite element method of analysis for studying the problem of sea ice indentation in the creeping mode of deformation. The analysis strategy, applicable to general viscoplastic behavior including creep (nonlinear viscoelasticity),

is based on a secant type iteration involving 4-6 cycles per time step on the global equations of motion and a Newton-Raphson, or tangent type iteration, combined with the α -method of time integration and typically not exceeding 4 cycles per time step, on the rate-dependent constitutive relations at each integration point within an element. The resulting computer code, called DECNEC, is capable of simulating a free or frictional contact between two deformable bodies, i.e., no contact stresses due to adfreeze bond, by defining the interface as a "slideline".

Numerical simulations of ice-structure interaction for a rigid cylindrical indenter under plane stress conditions, a problem of general interest for structural concepts in the Arctic, and an isotropic (von Mises) multi-axial power law creep model for sea ice showed that:

1. Global forces vary by a factor of 2.5 depending upon whether the interface condition is fixed (infinite adfreeze bond strength), roller, or free (no adfreeze bond strength or interface friction). The fixed condition is about 1.3 times and the free condition about 0.5 times the roller condition.
2. Finite element analysis predictions of global pressure differ from a (approximate) modified upper bound solution of Ting and Shyam Sunder⁷ by less than 10% for varying velocity, indenter diameter, and material constants.
3. The ratio of maximum normal interface pressure to global pressure approximately varies in the range 0.35-1.10 depending upon the interface condition. It is 0.35 for the fixed condition, 0.55 for the roller condition, and 1.10 for the free condition.
4. The maximum (peak) normal interface pressures vary by a factor of 1.26 depending upon the interface condition. The fixed condition is about 0.83 times and the free condition about 1.04 times the roller condition. The maximum interface shear stress for the fixed condition is about 0.81 times the corresponding maximum normal pressure. However, a different boundary value problem involving a smaller contact area, as opposed to contact over half the perimeter in the free condition, will lead to higher interface pressures.
5. Pressure-area curves should be considered as providing the maximum normal interface pressure for a given indenter area of contact (form area), rather than the average integrated normal pressure over a tributary loaded area for a structural component. It is conservative to assume a uniform or rectangular distribution of the local pressure over the indenter area of contact for purposes of design.
6. Tensile stresses, strains and strainrates occur almost all over the ice sheet, and may be the key to explaining fracture behavior during indentation. While biaxial compression and tension states tend to occur for stress on the upstream and downstream sides, respectively, the state of strain is almost always compression-tension. The levels of

tensile strain are often sufficient to cause cracking even before steady state creep is reached.

The possible effect of a grounded rubble pile or accreted ice foot on ice pressures was assessed by defining an effective indenter equal to a multiple (2.85) of the structural diameter. This resulted in a factor of 1.97 increase in global force. In the case of a grounded rubble pile, it would be overconservative to consider that all this force is transmitted to the foundation by the structure. On the other hand, the force transmitted to the foundation by the structure would decrease by a factor of 4.14 if both the structure and the grounded rubble pile could transmit a force proportional to the contact area of each with the foundation. This may be reasonable only if the rubble pile is consolidated and grounded firmly in the foundation soil such as in the case of constructed ice packs. Further research is necessary to quantify the level of force that can be directly transmitted to the foundation by a grounded rubble pile.

The numerical simulations also showed that (i) even a factor of two uncertainty in velocity will affect ice pressures only by about 20-30%, and (ii) uncertainties in material constants for an isotropic power law creep model may yield ice pressures that vary by about 15-30%. However, improved material models that include fracture and temperature effects in addition to the transversely isotropic behavior of sheet ice can have a major influence on ice pressure predictions. In particular, fracture in ice will be the key mechanism that limits ice pressures generated under the significantly higher velocities that occur in the field when compared with the value just prior to "breakout" or macrocracking considered here. This is an area for further research.

NOMENCLATURE

a	constant parameter in power law transformation matrix
B	finite element material compliance matrix
C	diameter of structure
D	elastic rigidity matrix
E	Young's modulus
G	transformation matrix for relating S to σ
K	elastic stiffness matrix of finite element
K _G	global stiffness matrix
n	power law exponent
P	global force acting on structure
Q	applied load vector
R	deviatoric stress vector
T	temperature
t	time or ice thickness
U	nodal displacement vector
V	approach velocity of ice sheet
W	parameter in time integrator
X	total strain vector
Y	inelastic strain vector
Z	creep strain vector
a	associative flow rule constant
b	Poisson's ratio
c	effective stress measure
d	stress vector
e	rate form is represented by a dot above the symbol

ACKNOWLEDGEMENTS

This research is funded by the Standard Oil Company (Ohio) through MIT's Center for Scientific

Excellence in Offshore Engineering, and cosponsored by the U.S. Department of the Interior, Minerals Management Service. The authors thank Jaideep Ganguly, graduate student, for computational assistance.

REFERENCES

1. Michel, S. and Toussaint, N., "Mechanisms and Theory of Indentation of Ice Plates," *Journal of Glaciology*, Vol. 19, No. 81, 1977, pp.285-300.
2. Croasdale, K.R., Morgenstern, M.R. and Nuttall, J.B., "Indentation Tests to Investigate Ice Pressures on Vertical Piers," *Journal of Glaciology*, Vol. 19, No. 81, 1977, pp.310-312.
3. Ralston, T.D., "An Analysis of Ice Sheet Indentation," *IAHR Ice Symposium*, Lulea, Sweden, 1978, pp.13-31.
4. Ponter, A.R.S. et al, "The Force Exerted by a Moving Ice Sheet on an Offshore Structure: Part I The Creep Mode," *Cold Regions Science and Technology*, Vol. 8, 1983, pp. 109-118.
5. Bruen, F.J. and Vivatrat, V., "Ice Force Prediction Based on Strain-Rate Field," *Third International Symposium on Offshore Mechanics and Arctic Engineering*, New Orleans, LA, 1984, 7 p.
6. Vivatrat, V. and Chen, V.L., "Ice Load Prediction with the Use of a Rate-Dependent Anisotropic Constitutive Law," *Proc. of the ASCE Specialty Conference: Arctic '85 - Civil Engineering in the Arctic Offshore*, San Francisco, California, March 1985, 11p.
7. Ting, S-K. and Shyam Sunder, S., "Sea Ice Indentation Accounting for Strain-Rate Variation," *Proc. of the ASCE Specialty Conference: Arctic '85 - Civil Engineering in the Arctic Offshore*, San Francisco, California, March 1985, 11p.
8. Baligh, M.M., "The Strain Path Method," *Research Report R84-01*, No. 761, Department of Civil Engineering, Massachusetts Institute of Technology, Cambridge, Massachusetts, Jan. 1984, 47 p.
9. Shyam Sunder, S. and Ting, S-K., "Ductile to Brittle Transition in Sea Ice under Uniaxial Loading," *Proc. of the 8th International Conference on Port and Ocean Engineering under Arctic Conditions*, Narssarsuaq, Greenland, Sept. 1985, 12 p.
10. Glen, J.W., "The Creep of Polycrystalline Ice," *Proc. of the Royal Society of London, Ser. A*, Vol. 228, No. 1175, 1955, pp.519-538.
11. Palmer, A.C., "Creep-Velocity Bounds and Glacier-Flow Problems," *Journal of Glaciology*, Vol. 6, No. 46, 1967, pp.479-488.
12. Snyder, M.D. and Bathe, K.J., "A Solution Procedure for Thermo-Elastic-Plastic and Creep Problems," *Nuclear Engineering and Design*, Vol. 64, 1981, pp. 49-80.
13. Hughes, T.J.R. and Taylor, R.L., "Unconditionally Stable Algorithms for Quasi-Static Elasto/Visco-Plastic Finite Element Analysis," *Computational Structural Mechanics*, Vol. 1, 1978, pp. 1-20.

14. Krieg, R.D., "Numerical Integration of Some New Unified Plasticity-Creep Formulations," SMIRT-4, M6/4, 1977.
15. Sanderson, T.J.O., "Theoretical and Measured Ice Forces on Wide Structures," Proc. 7th International Symposium on Ice, IAHR, Hamburg, August 1984, 32p.
16. Wang, Y.S., "A Rate-Dependent Stress-Strain Relationship for Sea Ice," First International Symposium on Offshore Mechanics and Arctic Engineering, New Orleans, 1982, pp. 243-248.
17. Gershunov, E.M., "Shear Strength of Adfreeze Bond and its Effect on Global Ice Load Applied to Mobile Offshore Drilling Units Under Arctic Conditions," Offshore Technology Conference, Paper OTC 4687, 1984, pp. 357-362.
18. Oksanen, P., "Friction and Adhesion of Ice," IAHR Ice Symposium, Quebec, Canada, 1981, pp.628-640.
19. Bruen, F.J., Byrd, R.C., Vivatrat, V. and Watt, B.J., "Selection of Local Design Ice Pressures for Arctic Systems," Offshore Technology Conference, Paper OTC 4334, 1982, pp. 417-435.
20. Sanderson, T.J.O., Personal Communications, 1984.
21. Frederking, R. and Gold, L.W., "Experimental Study of Edge Loading of Ice Plates," Canadian Geotechnical Journal, Vol. 12, No. 4, 1975, pp. 456-463.
22. Haynes, F.D., "Tensile Strength of Ice under Triaxial Stresses," USA CRREL Research Report 312, 1973, 21 p.

TABLE 1 - SUMMARY OF CASES

Case	Velocity (ft/hr)	Diameter (ft)	N	Interface Condition
1	0.64	350	3	Fixed
2	0.64	350	3	Roller
3	0.64	350	3	Free
4	0.10	350	3	Roller
5	1.00	350	3	Roller
6	0.64	1000	3	Roller
7	0.64	350	4	Roller

Note: 1 ft = 0.3048 m

TABLE 2 - SUMMARY OF RESULTS

Case	P/Dt (MPa)		Maximum Interface Normal Stress (MPa)	Maximum Effective Strainrate (s ⁻¹)
	Finite Element Analysis	Modified Upper Bound		
1	2.54	2.44	0.90	4.0x10 ⁻⁶
2	1.98	1.87	1.08	3.4x10 ⁻⁶
3	1.02	0.94	1.13	4.0x10 ⁻⁶
4	1.07	1.01	0.59	5.5x10 ⁻⁷
5	2.31	2.18	1.28	5.5x10 ⁻⁶
6	1.36	1.32	0.76	1.1x10 ⁻⁶
7	2.34	2.20	1.27	4.5x10 ⁻⁶

Note: Maximum Interface Shear Stress for Fixed Condition is 0.732 MPa
1 MPa = 145 psi

TABLE 3 - MULTIPLYING FACTORS FOR APPROXIMATE MODEL (Eq. 19)

Condition	Global Pressure	Maximum Interface Normal Stress
Roller	1.0	0.55
Fixed	1.3	0.46
Free	0.5	0.55

Note: Factor for Maximum Interface Shear Stress in
Fixed Condition = 0.37

TABLE 4 - PRINCIPAL STRESSES AT UPSTREAM TIP OF INDENTER

Case	Elastic (Time Step 1)		Steady State Creep (Time Step 20)	
	σ_z (MPa)	σ_y (MPa)	σ_z (MPa)	σ_y (MPa)
1	-0.19	-0.07	-0.90	-0.39
2	-0.30	+0.07	-1.08	-0.16
3	-0.36	+0.10	-1.13	-0.16
4	-0.18	+0.04	-0.59	-0.09
5	-0.35	+0.08	-1.28	-0.20
6	-0.11	+0.03	-0.76	-0.10
7	-0.31	+0.08	-1.27	-0.26

Note: Tension is Positive
1 MPa = 145 psi

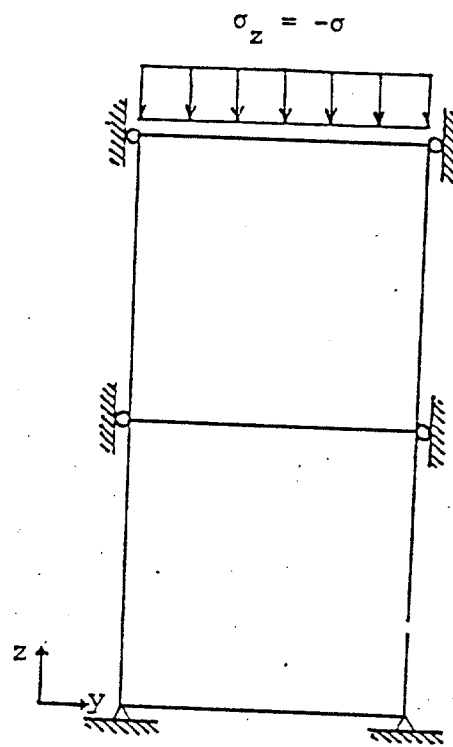


Fig. 1 - Test Problem

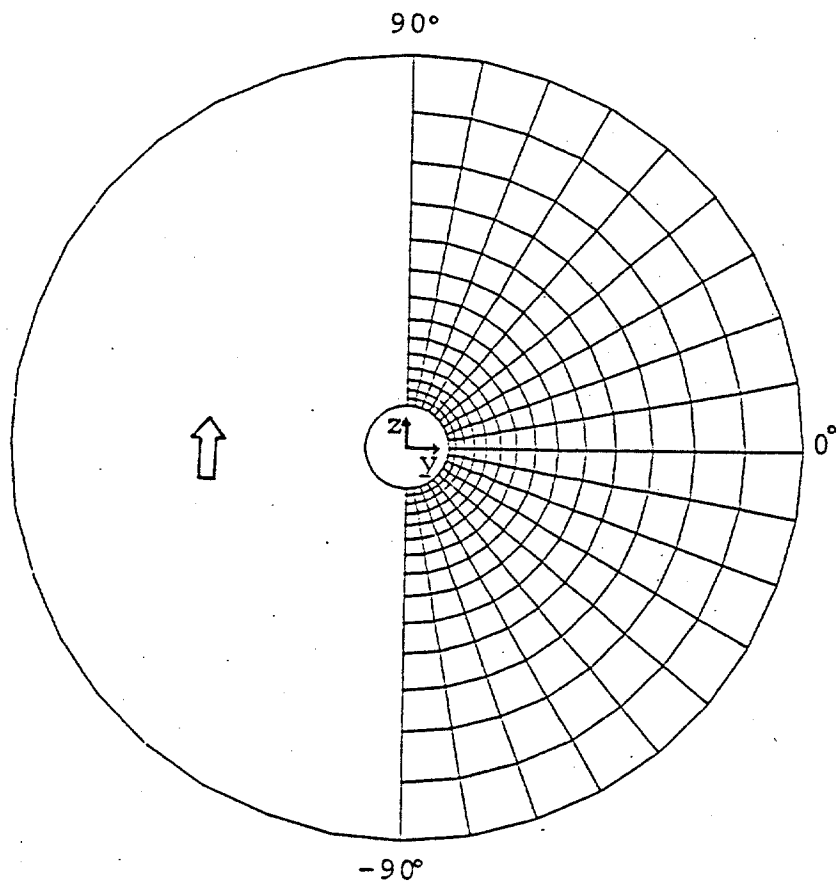
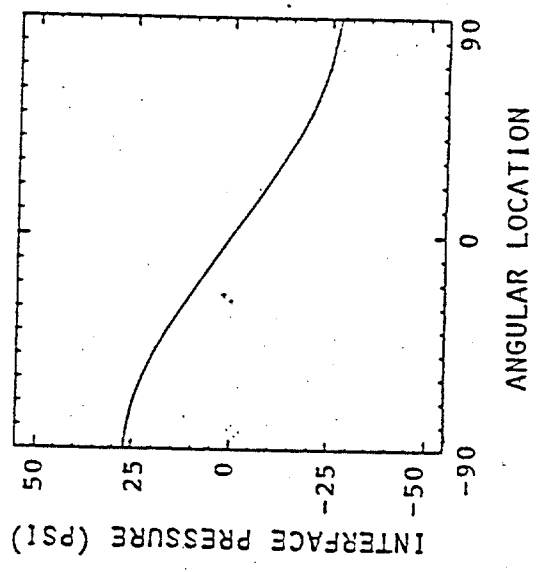
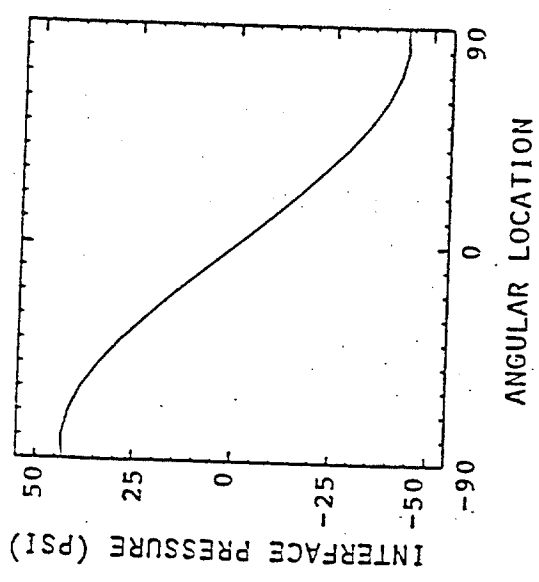


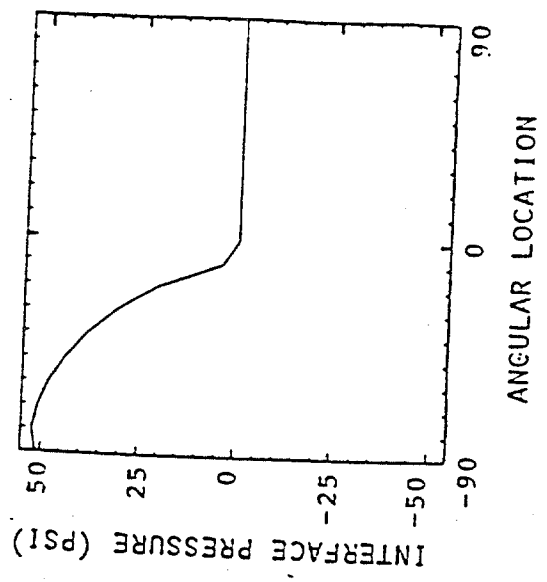
Fig. 2 - Finite Element Grid



(a) Fixed Condition

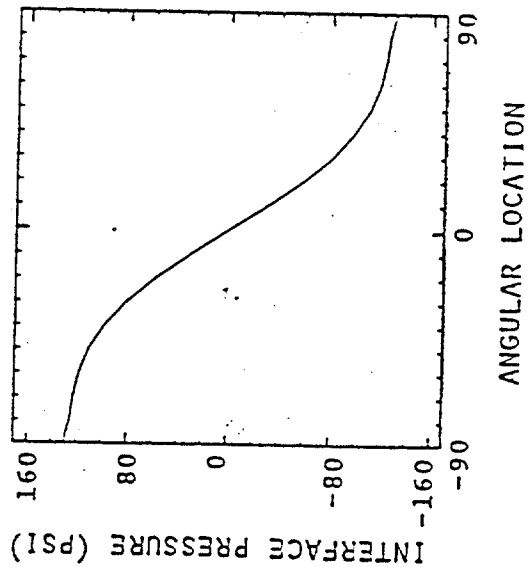


(b) Roller Condition

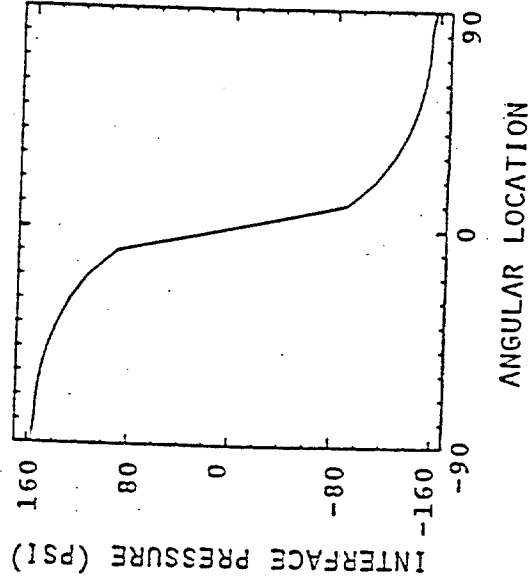


(c) Free Condition

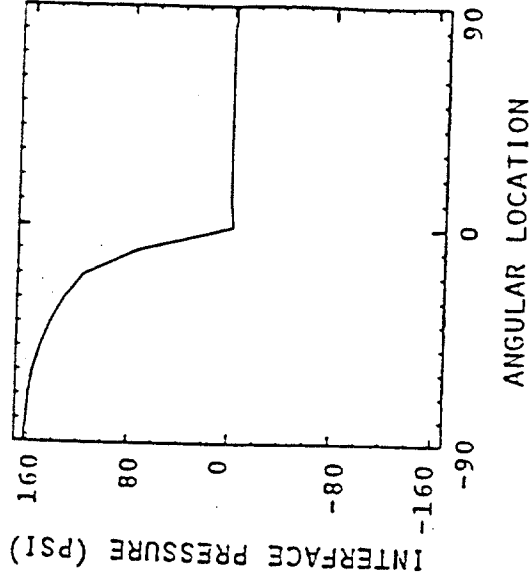
Fig. 3 - Normal Stress Distribution on Interface (Time Step 1)



(a) Fixed Condition



(b) Roller Condition



(c) Free Condition

Fig. 4 - Normal Stress Distribution on Interface (Time Step 20)

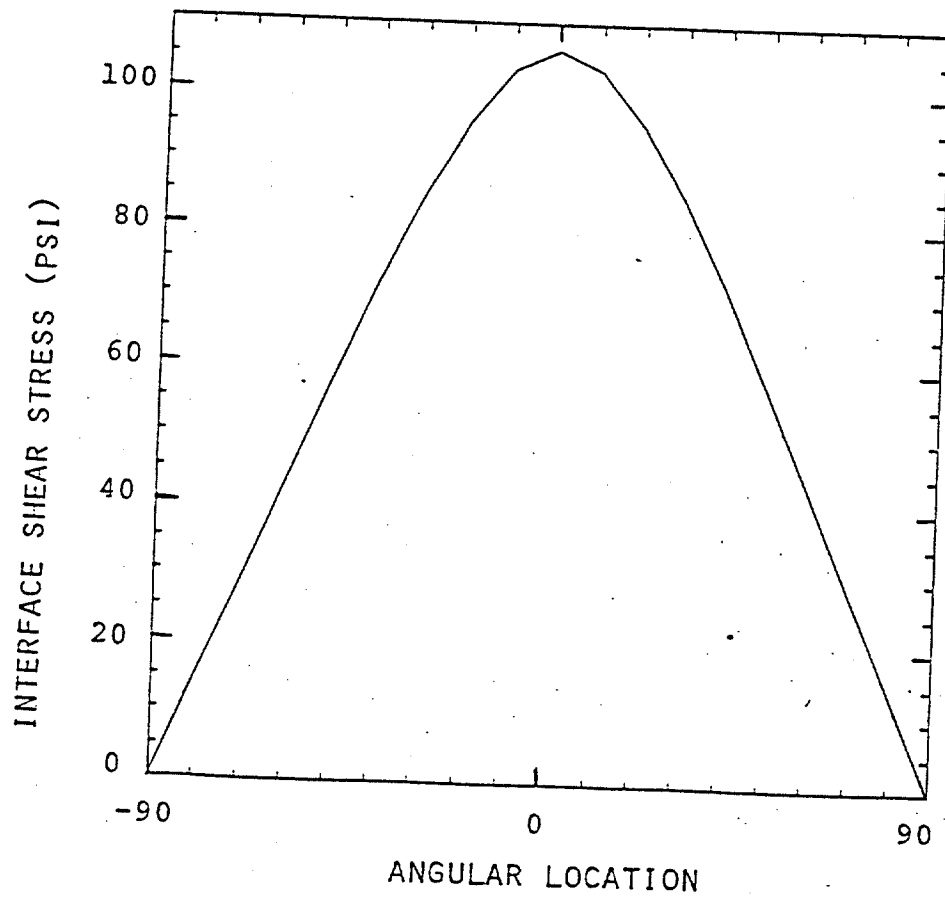


Fig. 5 - Shear Distribution on Interface for Fixed Condition
(Time Step 20)

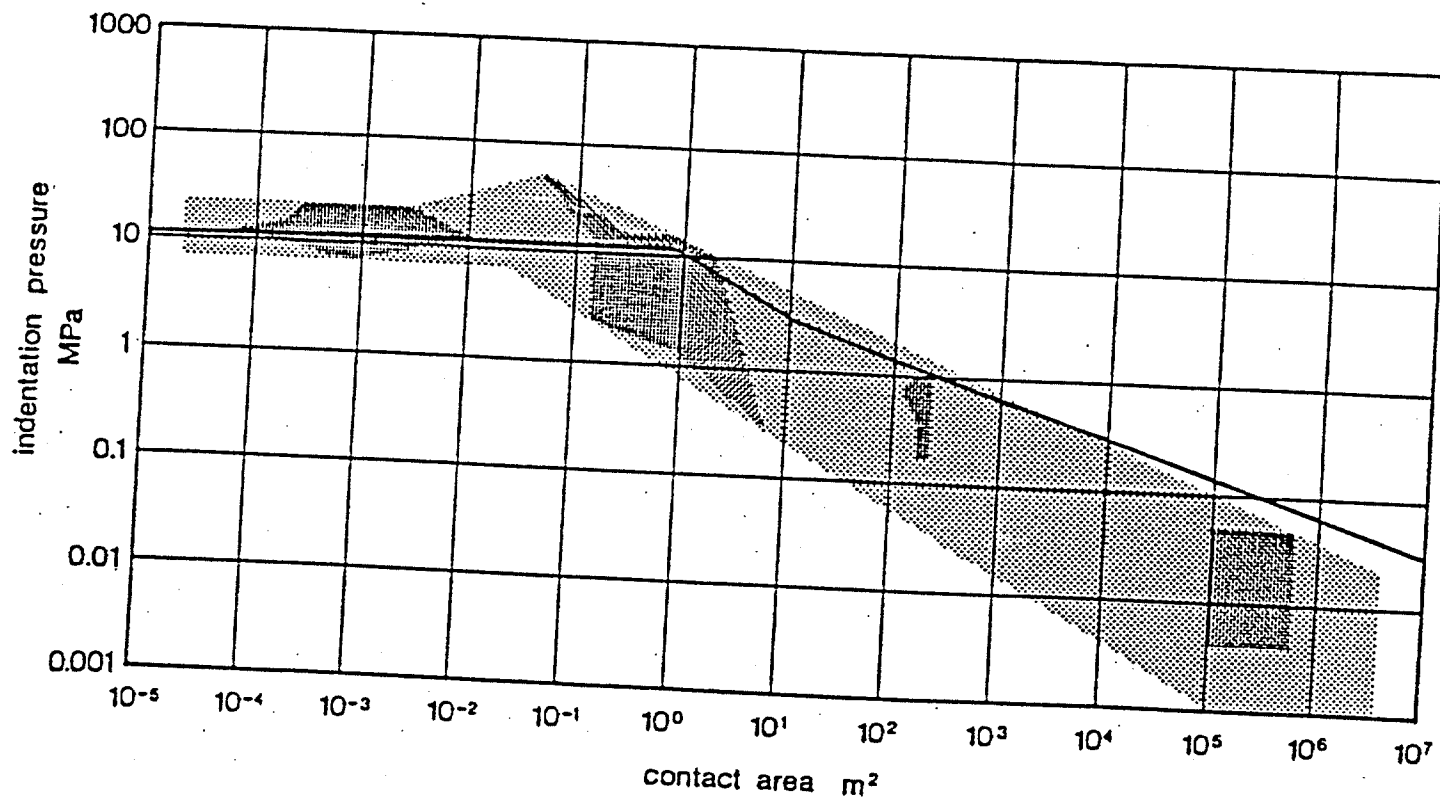
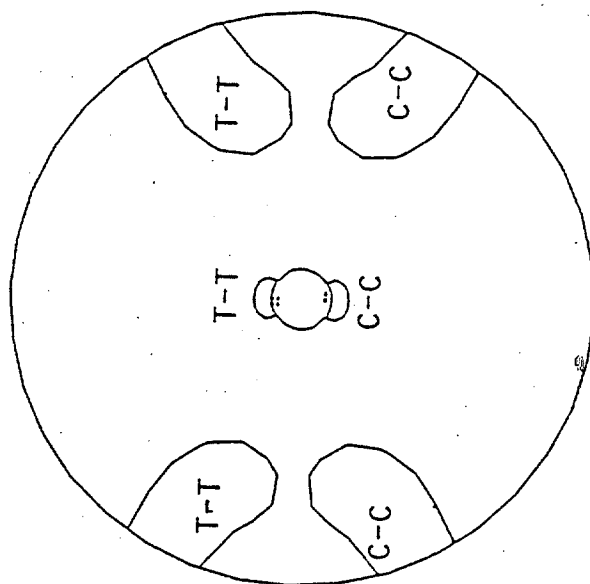
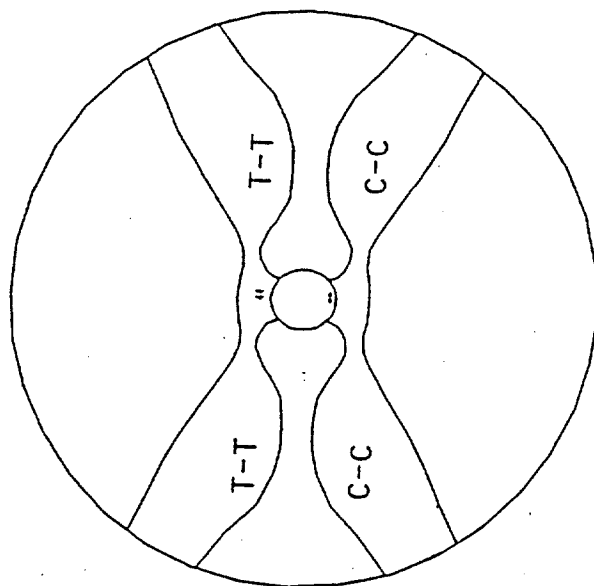


Fig. 6 - Pressure-Area Curve

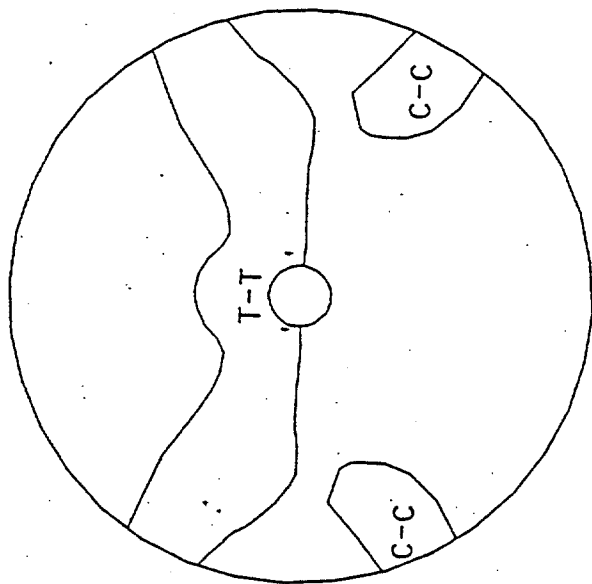


(a) Time Step 1

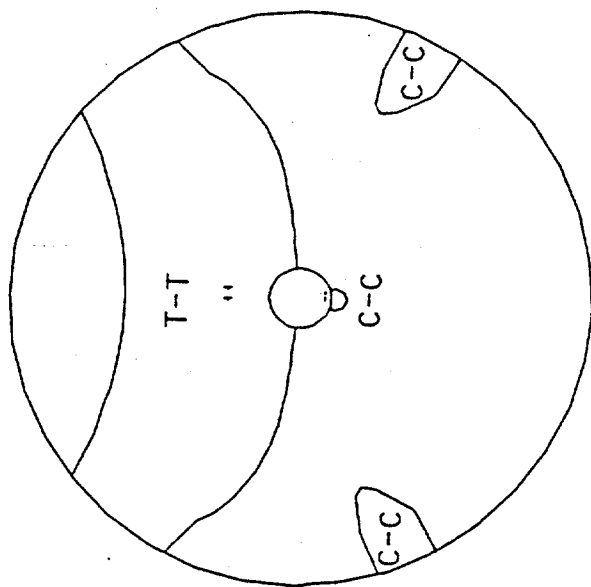


(b) Time Step 20

Fig. 7 - Biaxial Stress Regions for Fixed Condition



(a) Time Step 1



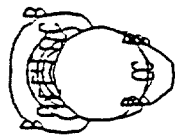
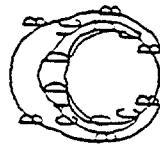
(b) Time Step 20

Fig. 8 - Biaxial Stress Regions for Free Condition

Maximum Principal Strain

Contour Levels

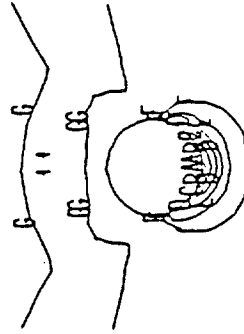
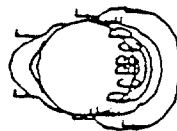
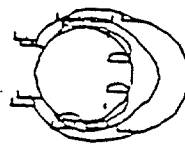
A = 0.0
 B = 0.0005
 C = 0.0010
 D = 0.0015
 E = 0.0020
 F = 0.0025



Minimum Principal Strain

Contour Levels

A = -0.0030
 B = -0.0025
 C = -0.0020
 D = -0.0015
 E = -0.0010
 F = -0.0005
 G = 1.2×10^{-10}



(a) Fixed

(b) Roller

(c) Free

Fig. 9 - Principal Strain Contours (Time Step 20)

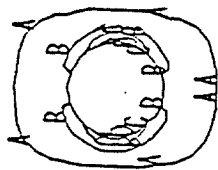
Contour Levels

A = 0.5×10^{-6}

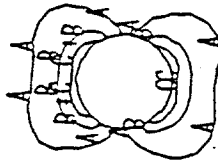
B = 1.5×10^{-6}

C = 2.5×10^{-6}

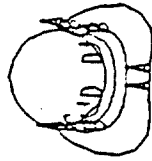
D = 3.5×10^{-6}



(a) Fixed



(b) Roller



(c) Free

Fig. 10 - Effective Strainrate Contours (Time Step 20)